THE ASTROPHYSICAL JOURNAL, 532:628–647, 2000 March 20

YOHKOH SXT AND *SOHO* EIT OBSERVATIONS OF SIGMOID-TO-ARCADE EVOLUTION OF STRUCTURES ASSOCIATED WITH HALO CORONAL MASS EJECTIONS

ALPHONSE C. STERLING[1,2]
Computational Physics, Inc., 2750 Prosperity Avenue, Suite 600, Fairfax, VA 22031, and E.O. Hulburt Center for Space Research, Naval Research Laboratory, Washington, DC; asterling@solar.stanford.edu

HUGH S. HUDSON[3]
Solar Physics Research Corporation, 4720 Calle Desecada, Tucson, AZ 85718; hhudson@solar.stanford.edu

BARBARA J. THOMPSON
NASA/GSFC Code 682, Greenbelt, MD 20771; barbara.thompson@gsfc.nasa.gov

AND

DOMINIC M. ZARRO
SM&A/Systems Solutions Group and NASA/GSFC Code 682.3, Greenbelt, MD 20771; dzarro@solar.stanford.edu
Received 1999 June 14; accepted 1999 October 22

ABSTRACT

A subset of the solar-disk counterparts to halo coronal mass ejections (CMEs) displays an evolution in soft X-rays (SXR) that is characterized by a preflare S-shaped structure, dubbed a "sigmoid," which evolves into a postflare cusp or arcade. We examine the morphological properties of the evolution of sigmoids into cusps and arcades for four such regions associated with SXR flares, using the Soft X-Ray Telescope (SXT) on the *Yohkoh* satellite and the EUV Imaging Telescope (EIT) on the *Solar and Heliospheric Observatory* (*SOHO*) satellite. Most of our EIT observations are with the 1.5 MK 195 Å Fe XII channel. At most, there is only a weak counterpart to the SXR sigmoid in the preflare 195 Å EUV images, indicating that the preflare sigmoid has a temperature greater than 1.5 MK. While more identifiable than in the 195 Å channel, a clear preflare sigmoid is also not observed in the 2.0 MK EIT 284 Å Fe XV channel. During the time of the flare, however, an EUV sigmoid brightens near the location of the SXR preflare sigmoid. Initially the SXR sigmoid lies along a magnetic neutral line. As the SXR flare progresses, new field lines appear with orientation normal to the neutral line and with footpoints rooted in regions of opposite polarity; these footpoints are different from those of the preflare sigmoid. The cusp structures in SXRs develop from these newly ignited field lines. In EIT images, the EUV sigmoid broadens as the flare progresses, forming an arcade beneath the SXR cusp. Our findings are consistent with a standard picture in which the origin of the flare and CME is caused by the eruption of a filament-like feature, with the stretching of field lines producing a cusp. We infer that the cusp-producing fields may be overlying the sigmoid fields in the preflare phase, but we do not directly observe such preflare overlying fields.

Subject headings: Sun: corona — Sun: flares — Sun: particle emission — Sun: UV radiation — Sun: X-rays, gamma rays

1. INTRODUCTION

There is a keen interest in coronal mass ejections (CMEs) among solar and geophysical scientists, as they are a primary mechanism by which the material and magnetic fields of the Sun's atmospheric layers directly interact with the Earth. It is well known that these interactions can have substantial consequences on the geomagnetic environment of the Earth, sometimes resulting in power disruptions or damage to satellites (e.g., McAllister et al. 1996; Berdichevsky et al. 1998). Identifying the low-altitude coronal sources of coronal mass ejections (CMEs) is vital to understanding their ejection mechanism and, eventually, in being able to forecast when the eruptions will occur. Some recent reviews of CMEs are by Kahler (1992), Hundhausen (1993), Gosling (1996), Low (1997); and Hudson & Webb (1997).

It has proven a challenge to determine the locations of CME source regions in the low corona unambiguously. In particular, the CMEs that are easiest to see with coronagraphs are those that are in the plane of the sky, i.e., those ejected normal to the Earth-Sun line of sight (Hundhausen 1993). Thus, the most readily visible CMEs originate preferentially from the limb of the Sun. Low-altitude coronal source regions for these CMEs would often be seen in projection at the limb, thereby precluding clear views of the coronal features responsible for the eruptions (e.g., Rust & Hildner 1976; Dere et al. 1997). Various features are commonly used as indirect indicators of CMEs on the disk. These include prominence eruptions, long-duration soft X-ray (SXR) flares, SXR and EUV arcade formation, and SXR and EUV "dimming" or transient coronal holes (cf. above-cited reviews). Use of such proxies, however, is not always easy or definitive in identifying CMEs.

The class of CMEs known as "halo" CMEs offers particularly promising chances for identifying CME sources in the low corona. Such CMEs, first noted by Howard et al. (1982) in *P78-1* data, appear as a halo fully or nearly fully surrounding the coronagraph's occulting disk. In such

[1] Current address: NASA/Marshall Space Flight Center, SD50/Space Science Department, Huntsville, AL 35812.
[2] Currently an NRC-MSFC Research Associate.
[3] Current address: Institute for Space and Astronautical Science, Yoshinodai 3-1-1, Sagamihara, Kanagawa 229-8510, Japan.

events, the CME moves either directly toward the Earth, or directly away. Therefore, one expects that approximately 50% of halo CMEs have source regions visible on the disk of the Sun as observed from the near-Earth environment.

With the Soft X-Ray Telescope (SXT) on *Yohkoh*, we have recently identified coronal regions in soft X-rays that are the source locations of (or at least regions closely linked to the source regions of) halo CMEs observed with the Large Angle Spectrometric Coronagraph (LASCO) set of coronagraphs on *SOHO*. Sterling & Hudson (1997) initially studied the source region for a well-observed halo CME of 1997 April 7 (e.g., Berdichevsky et al. 1998; Kaiser et al. 1998; and Thompson et al. 1999). Hudson et al. (1998) extended that investigation to eleven halo CMEs, including the 1997 April 7 event. Six of these eleven halo CMEs had solar-disk manifestations detectable in SXT, and four had no apparent on-disk counterpart, consistent with approximately 50% of the halos CMEs originating on the farside of the Sun. For the one remaining halo event, SXT data coverage was too poor to make a determination (although independent data indicate that it occurred on the Earthward side of the Sun; see Table 1 in Hudson et al. 1998).

Of the six Hudson et al. (1998) events with clear disk counterparts, four showed a similar behavior: a preeruption active region structure, initially twisted into an S-shape, which evolved into a posteruption cusp-shaped or arcade structure. We denote the S-shaped structures "sigmoids," based on descriptions of them as sigmoid features by Rust (1996) and Rust & Kumar (1996), and we describe these events as displaying a "sigmoid-to-arcade" evolution. Although in at least three cases the preflare sigmoids existed more or less intact for some days prior to eruption (the 1997 May 21 region was only mildly sigmoidal), the sigmoid-to-arcade evolution occurred over a few hours and was accompanied by a soft X-ray flare in the active region. Plunkett et al. (1998) and Thompson et al. (1998) also discuss one of these events that occurred on 1997 May 12. One of the remaining two Hudson et al. events with disk counterparts (the event of 1997 February 7) showed a similar pattern but was accompanied by a huge quiet-region arcade not observed in the above four cases. The sixth of the Hudson et al. events (1997 January 6) originated from a very inconspicuous diffuse region structure that did not show the pattern of the four sigmoid-to-arcade events. This event, and its geophysical consequences, is discussed by Burlaga et al. (1998); Fox, Peredo, & Thompson (1998); Reiner et al. (1998); Webb et al. (1998); and Watari & Watanabe (1998). It was an important event because it illustrates that the sigmoid-to-arcade pattern is not universal and that some geophysically important CMEs can occur even without exhibiting such a pattern in SXRs.

Since the *Skylab* mission, it has been suspected that CMEs (or, "coronal transients," to use the jargon of that day) are related to SXR structures that change from a system of nonpotential magnetic loops to potential magnetic loops (e.g., Kahler 1977). Sheeley et al. (1975) observed a "sinuous emission feature" that changed form with the suspected ejection of a coronal transient. Similar patterns have been seen frequently in SXT data (e.g., Sakurai et al. 1992; Manoharan et al. 1996) and their possible connection to CMEs extensively discussed (e.g., Rust & Kumar 1996; Chen 1997; Rust 1997). Cusp-shaped features are commonly observed by SXT (e.g., Tsuneta et al. 1992). Consequently, there is much evidence that the sigmoid-to-arcade pattern of CME-associated soft–X-ray structures is not a rare phenomenon and may be a fundamental aspect of many CMEs.

To study the sigmoid-to-arcade evolution, Sterling & Hudson (1997) and Hudson et al. (1998) used "difference images," whereby a pre-event image was subtracted from a post-event image. Zarro et al. (1999) combine difference images from SXT and EIT to investigate the flaring region associated with the 1997 April 7 halo CME. Thus, in the four sigmoid-to-arcade Hudson et al. (1998) events, and in the two separate 1997 April 7 event studies, the analysis was confined to images of only the pre-event sigmoid structure and the post-event cusp or arcade structure so that the evolution in between was not examined. This paper investigates the morphology and temporal evolution of the sigmoid into the cusp or arcade, using both SXT and EIT data, for the four events showing this pattern in Hudson et al. (1998).

2. INSTRUMENTATION AND DATA

Hudson et al. (1998) examined events from a list of halo CMEs that occurred during the period from 1996 December 19 to 1997 May 21 (O. C. St. Cyr, 1997, private communication). These halo CMEs were observed with LASCO (Brueckner et al. 1995; Howard et al. 1997). Based on those events, we examine the CME source regions in soft X-rays using *Yohkoh* SXT. SXT uses four analysis filters spanning the approximate wavelength range 3–45 Å, effectively detecting coronal plasmas at temperatures $\gtrsim$2–3 MK. We use two of the "thinner" filters, viz., the Al.1 and MgAl filters, and base our analysis on 4.″91 or 9.″82 pixel SXT full-frame images that view the whole Sun. Unlike the SXT partial-frame images, which have a restricted field of view, the full frames allow us to select subimages sufficient to view structures of interest. Many of the images are composites of images with varying exposure durations ranging from 0.037 to 7.58 s. These composite images provide the highest dynamic range while avoiding saturation of the brightest features; such images are ideal for following the morphological evolution of the structures. Intensities in these composite images are normalized allowing for quantitative calculations of fluxes and temperatures (Tsuneta et al. 1991).

SOHO EIT (Delaboudiniere et al. 1995) produces full-Sun images with a spatial resolution of 2.″6 in four EUV wavelength bands, each covering a narrow wavelength range sensitive to the lower corona. We primarily use the 195 Å Fe XII filter, which detects emission from approximately 1.5 MK coronal plasmas, thus sampling cooler material than the corresponding SXT images. Most of our EIT images have exposure durations of 3.8 or 9.1 s. We compare images from EIT and SXT with magnetograms obtained from the *SOHO* Michelson Doppler Imager (MDI; Scherrer et al. 1995).

The present analysis focuses on the four halo CME events that Hudson et al. (1998) found to show a clear sigmoid-to-arcade development. These events are (1) a *GOES*-class C2 event of 1996 December 19, with maximum *GOES* soft X-ray flux near 15:56 UT; (2) the *GOES*-class C7 event of 1997 April 7, with maximum near 14:03 UT; (3) a *GOES*-class C1 event of 1997 May 12, with maximum near 04:52 UT; and (4) a *GOES*-class M1 event of 1997 May 21, with maximum near 20:08 UT. We show *GOES* profiles for these four events in Figure 1, with times of *Yohkoh* space-

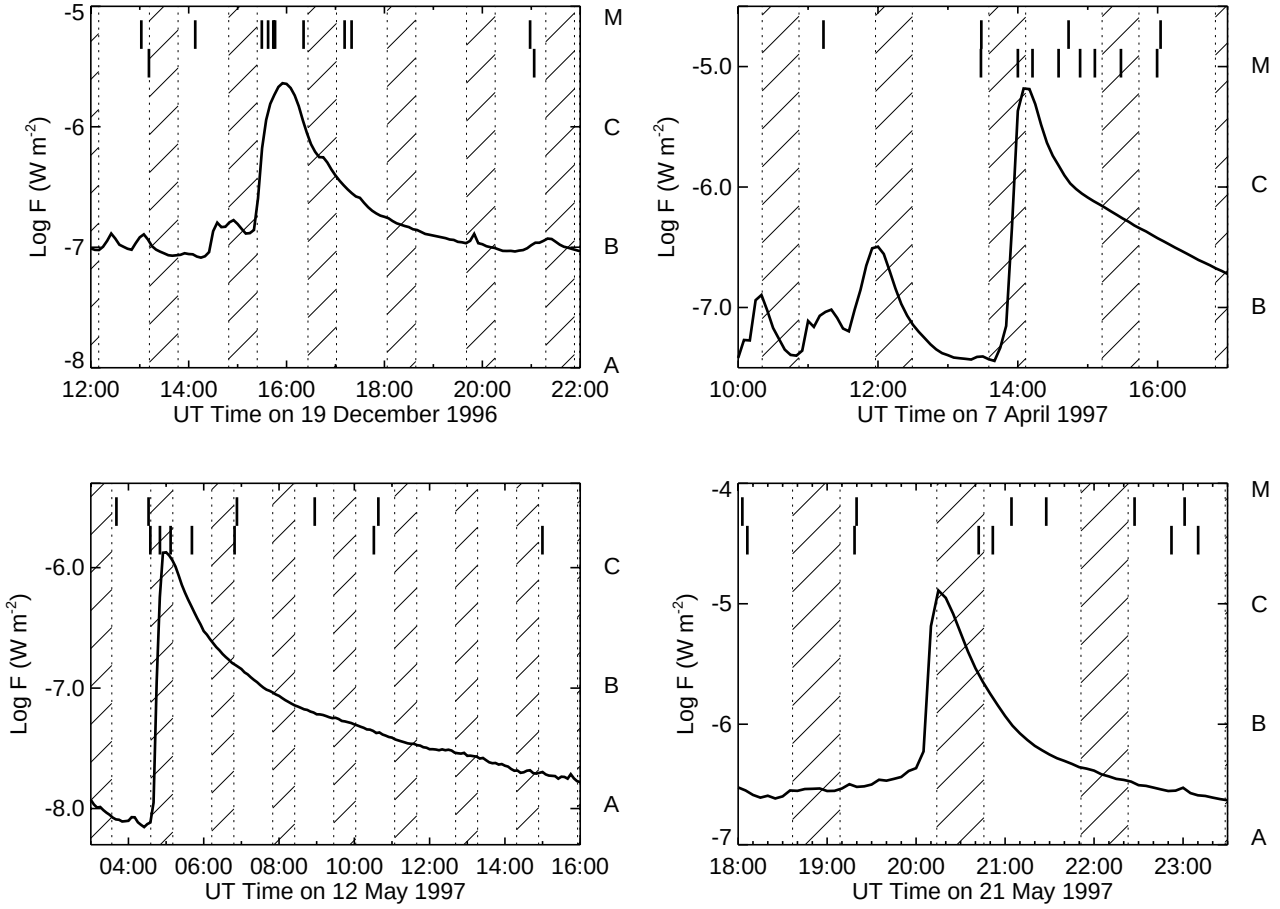

FIG. 1.—*GOES* profiles for the four events of this study. Hatched areas represent times of *Yohkoh* spacecraft night. Across the top of each panel, the upper set of tick marks show the times of the SXT images and the lower set of tick marks show the times of the EIT images in Figs. 2, 3, 4, and 5.

craft night indicated. Since *SOHO* is located at Lagrangian point L1, it does not undergo spacecraft night.

Prior to 1997 September there was a timing problem with EIT, and the onboard clock could be several minutes ahead of "real" time. Unfortunately, there is no way to recover this discrepancy. However, the onboard time always ran ahead of real time. Therefore the times we give for EIT in the text and in the figures for all four of these events will either be the correct times or within a few minutes ahead of the correct time. SXT times are correct.

3. MORPHOLOGICAL EVOLUTION

We examine the morphology of each event in chronological order of occurrence. We show the results for SXT and EIT for each event in Figures 2, 3, 4, and 5 in a total of 12 panels per event, with the number of images from the two instruments for each event varying depending on data coverage.

3.1. *1996 December 19 Event*

Since this event had sparse EIT coverage, we can only follow the region's evolution in detail with SXT. Figure 1*a* shows that SXT tracked the evolution from the rise phase to past the peak of the corresponding soft X-ray flare. Figure 2 shows SXT images at various times during the evolution, beginning in Fig. 2*a* and continuing through Fig. 2*j*. Figures 2*k* and 2*l* show EIT 195 Å images from before and after the flare, respectively. An S-shaped sigmoid is clearly evident in the SXT images during the preflare phase in Figures 2*a* and 2*b*. A portion of the sigmoid near the center of the images shows enhanced intensity. It is from this portion of the sigmoid that the transformation into a postflare arcade begins, coincident with the initiation of the SXR flare in Figure 2*c*. This flare-associated arcade brightening does not appear to be a part of the preflare sigmoid itself but, rather, a new, independent feature. As the development progresses, the brightening of the new arcade continues in Figures 2*d*–2*g*, perhaps spreading to other loops, although this is unclear owing to saturation of the brightest pixels in those images.

By the time of Figure 2*h*, the post-event arcade structure is beginning to dim. It maintains its general form for the duration of the event and persists in this general form for some time (cf. SXT image of Fig. 2*j*).

Figure 2*k* shows a pre-event EIT image, corresponding approximately in time to the SXT image in Figure 2*a*. Figure 2*l* shows a post-event EIT image at approximately the time of the SXT image in Figure 2*j*. There is no evidence of the preflare sigmoid seen in the SXT images in the pre-event EIT image. There is, however, an EUV manifestation of the postflare structures in the EIT images at 21:03 similar to two Hα flare ribbons denoting the footpoints of the SXR arcade. Figures 2*a* and 2*k* show virtually no similarity, while Figures 2*j* and 2*l* show a relatively strong similarity.

We make direct comparisons between the SXT and EIT images for this event in the top row of Figure 6. Figure 6*a* shows the EIT preflare image, while Figures 6*b* and 6*c* show

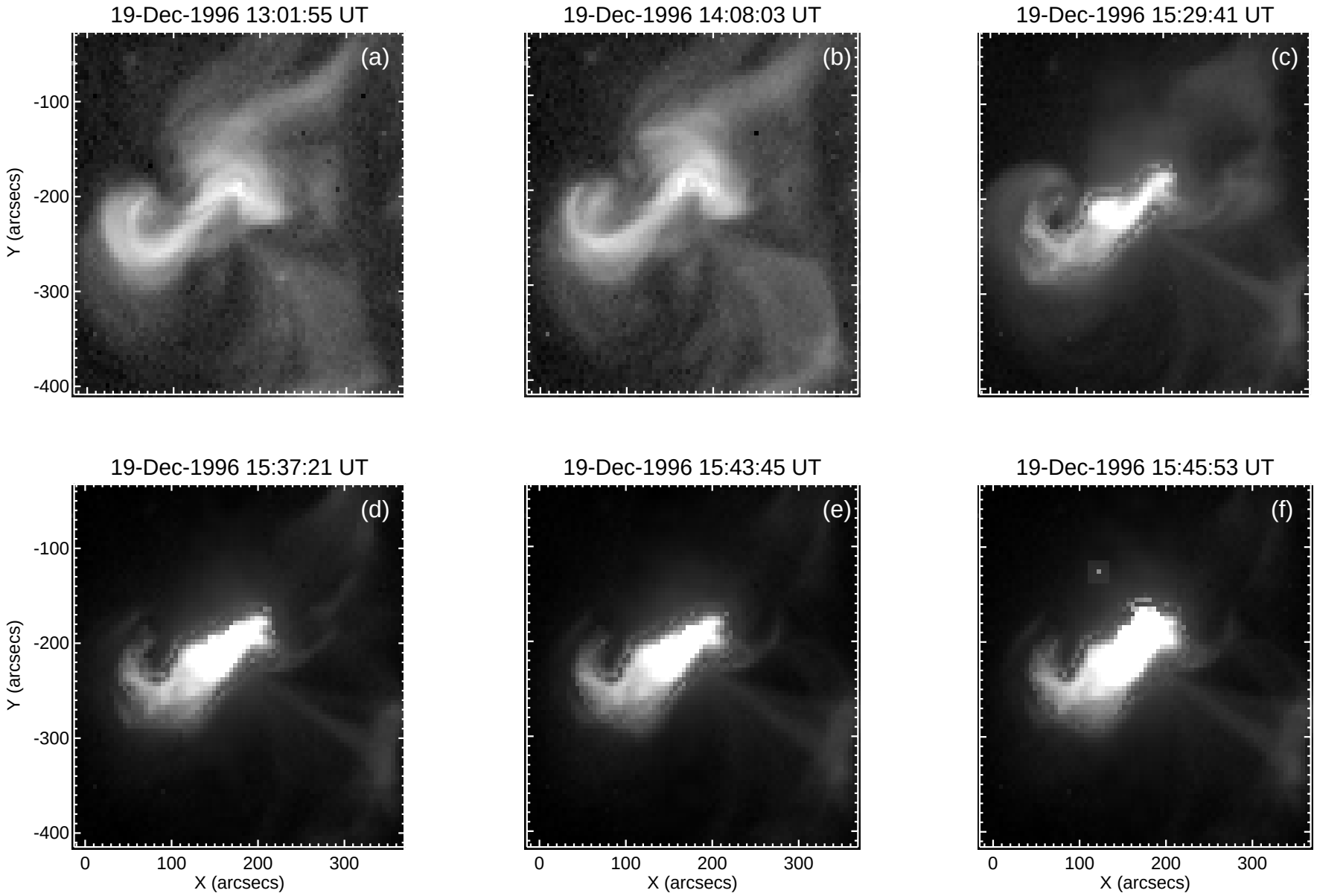

FIG. 2.—Evolution of the 1996 December 19 event in SXRs in (*a*)–(*j*), and in EUV (195 Å) in (*k*) and (*l*). Size scales are listed in arcseconds, where the values are calibrated to solar-disk center. North is the top and east is to the left in these images and in all the images in the subsequent figures.

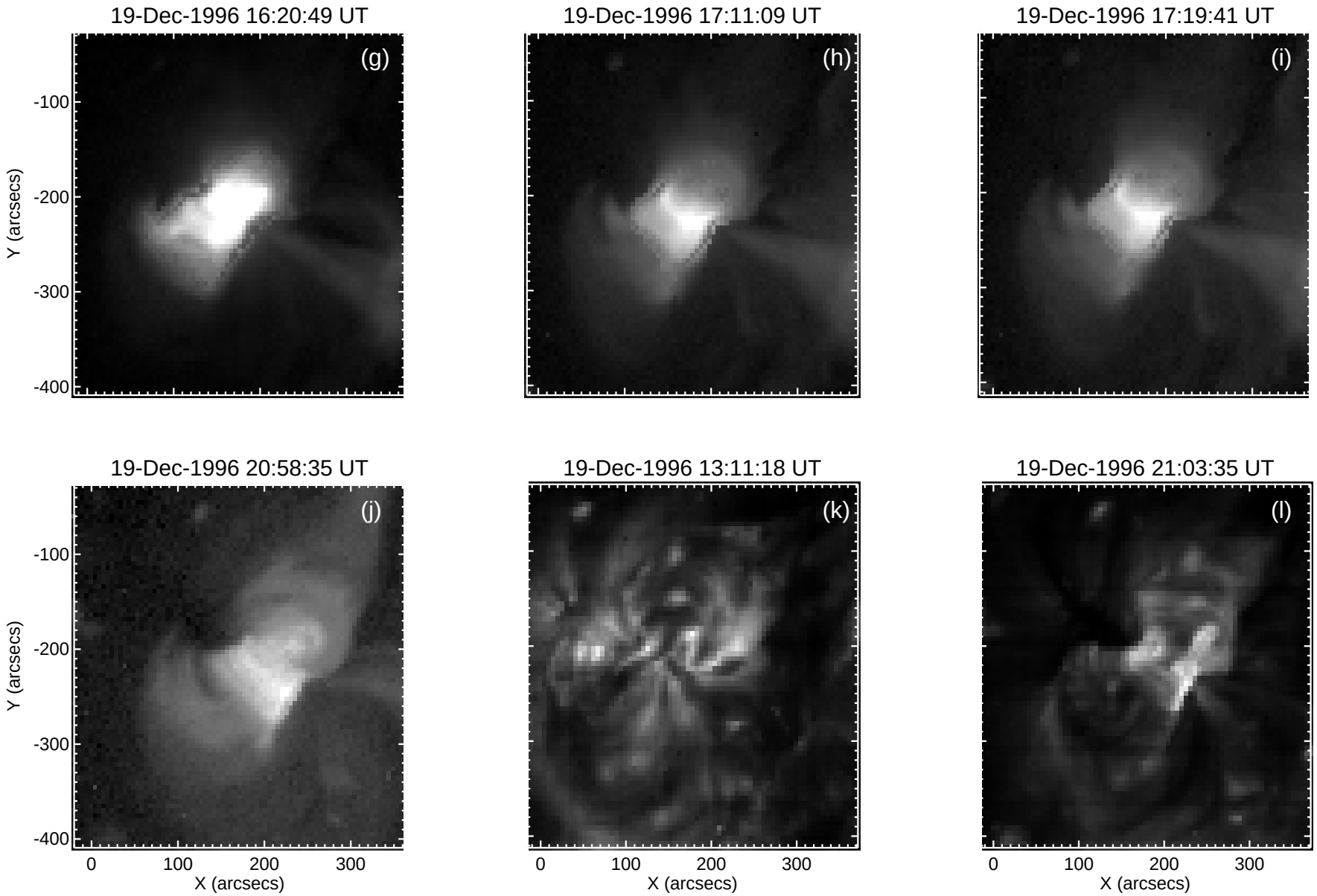

FIG. 2.—*Continued*

the postflare EIT image. Overlaid in orange or red on each image are SXR contours. Orange contours are from preflare times, specifically, the SXT time listed above the leftmost panel (Fig. 6*a* in the *a–c* grouping). In the middle and rightmost figures (Figs. 6*b* and 6*c* in this grouping) red contours are for SXT images near the peak and during the decay phase of the flare, respectively. Also overlaid on Figures 6*a* and 6*c* are magnetogram contours from MDI, with purple and yellow indicating opposite polarities.

Figure 6*a* shows that the preflare sigmoid of Figures 2*a* and 2*b* runs along the neutral line. During the flare, from the red contours in Figure 6*b* (corresponding in time to Fig. 2*c*), we infer that the new loops being formed in SXR have footpoints in the yellow polarity region (cf. Figs. 6*a* and 6*c*). By the time of the SXR contours in Figure 6*c* (corresponding to Fig. 2*i*), it is clear that this new arcade is anchored with one side in each polarity region and that it runs normal to the direction of the preflare sigmoid.

3.2. *1997 April 7 Event*

As indicated in Figure 1*b*, *Yohkoh* missed the rise phase of this event because of spacecraft night, but coverage with EIT was better than in the previous event. Figures 3*a–3d* and Figures 3*e–3l* show SXT images and EIT 195 Å images, respectively.

As discussed in Sterling & Hudson (1997), Hudson et al. (1998), and Zarro et al. (1999), the SXT preflare images show a characteristic sigmoidal structure, while the near-peak and postflare SXT images show a distinct cusp-shaped feature. Unlike SXT, EIT does not show a distinct structure, but rather the corresponding feature is composed of a much more complex pattern of loops (Zarro et al. 1999). The detail visible in EIT compared with SXT is, in part, owing to the higher resolution of the EIT images used.

There are intensity enhancements at various locations in the preflare EIT image of Figure 3*e*, and additional brightenings occur along what appear to be tightly twisted loops in Figure 3*f*. Figure 3*g* shows that the major flare brightening erupts near this location, with the brightest pixels being saturated in Figures 3*g* and 3*h*. In the latter two figures, a sigmoid-like structure becomes apparent at the same location as, and with similar orientation to, the preflare SXR sigmoid. This EUV sigmoid is not prominent until around the time of the peak of the soft X-ray flare. Zarro et al. (1999) pointed out a dark filament in the preflare EIT image in Figure 3*e*. In Figures 3*f–3h*, plasma near this location brightens into the EUV sigmoid, indicating that a filament, a part of a filament, or a filament channel brightens and erupts. After the brightening subsides, a structure that appears to be less complicated magnetically than the preflare structure remains (Figs. 3*j–3l*) and appears situated below the bright cusp in SXRs (Figs. 3*c* and 3*d*). Figures 3*i–3l* indicate that the EUV region broadens as if it were a set of expanding loops. Eventually, the EUV sigmoid and other intense EUV brightenings fade, although a new set of loops remains enhanced in intensity (Fig. 3*l*).

Figures 6*d–6f* show overlays between EIT, SXT, and MDI magnetograms for this event. As was the case in the 1996 December 19 event, the preflare SXR sigmoid (Fig. 6*d*) is aligned along the magnetic neutral line to within the uncertainties caused by projection effects. The SXR sigmoid is approximately aligned with portions of the preflare structure visible in EUV. As in the December 19 event, this feature does not stand out enough from the surrounding material to appear as a prominent sigmoid in EUV before the flare begins. Figure 6*e* overlays two SXT images onto an EIT image during the flare. Orange and red contours show a preflare image and an image from near the flare's peak, respectively. The preflare overlay indicates a close connection between the EUV sigmoid-type brightening of Figures 3*g* and 3*h* and the preflare SXR sigmoid of Figures 3*a* and 3*b*. Figure 6*f* shows overlays of the region during the late decay phase for both EIT and SXT, with the cusp-shaped SXR feature enveloping a noncusped EUV loop and both features seemingly anchored in opposite-polarity regions (cf. Zarro et al. 1999).

3.3. *1997 May 12 Event*

Yohkoh missed the rise phase of this event because of spacecraft night. Since the event was long-lived, we follow its evolution during the long decay phase. Figure 4 shows SXT images in the first five panels and EIT 195 Å images in the last seven panels. Figures 4*a* and 4*b* show a preflare SXT sigmoid (actually, an inverted S in this case) that hints at a complex geometry perhaps consisting of interlaced loops. By the time of the first postflare image in Figure 4*c*, the region around the bright preflare sigmoid loops has reconfigured, and a faint extension from the region has developed. The latter emission appears to be caused by an arcade of low-lying loops extending from south to north, with a cusp-shaped feature pointing upward and running along the arcade. The arcade and enveloping cusp feature expands in the east-west direction as the event proceeds.

Figure 4*f* shows a preflare EIT image, indicating complex loop structures that (unlike the December 19 and April 7 cases) have a sigmoidal shape similar to the SXT preflare images. The EIT preflare sigmoid does not stand out from its surroundings as much as the SXT preflare sigmoid does. As the flare begins in Figure 4*g*, a long, narrow contorted structure brightens. The emission subsequently brightens most in a concentrated area (Fig. 4*g*), which then expands in both breadth (similar to the 1997 April 7 event) and northward into an extended arcade. Loop structures begin to "bubble out" from the northern edge of the arcade (clearly seen in Fig. 4*k*) and grow northward with time.

Figures 6*g–6i* overlay EIT, SXT, and MDI images. Figure 6*g* shows that the preflare SXT sigmoid does not exactly overlay the EIT preflare brightenings, but it does run near or along the neutral line in the MDI magnetograms. Early in the flare, the long, narrow brightening in EIT develops near the location of the SXR preflare sigmoid (Fig. 6*h*). Late in the event, the newly developed EUV loops lie within the bright SXR postflare cusp (Fig. 6*i*). We observed similar behavior in the 1997 April 7 case.

3.4. *1997 May 21 Event*

Figures 5*a–5f* and Figures 5*g–5l* show SXT and EIT 195 Å images, respectively, for the 1997 May 21 event. SXT preflare images show a weak sigmoid-shaped brightening in Figures 5*a* and 5*b*. During the late decay, the region forms a set of bright loops. Although a cusp shape is not unambiguous, the appearance of the brightest portion of the arcade is consistent with a cusp pointed nearly along the Sun-Earth line of sight (Figs. 5*c* and 5*d*; cf. the theoretically calculated appearance of cusps in Fig. 15*i* of Forbes & Acton 1996). The east side of this loop (or cusp) fades more quickly than the west side (Figs. 5*e* and 5*f*). As in the December 19 and April 7 events, the EIT images show no

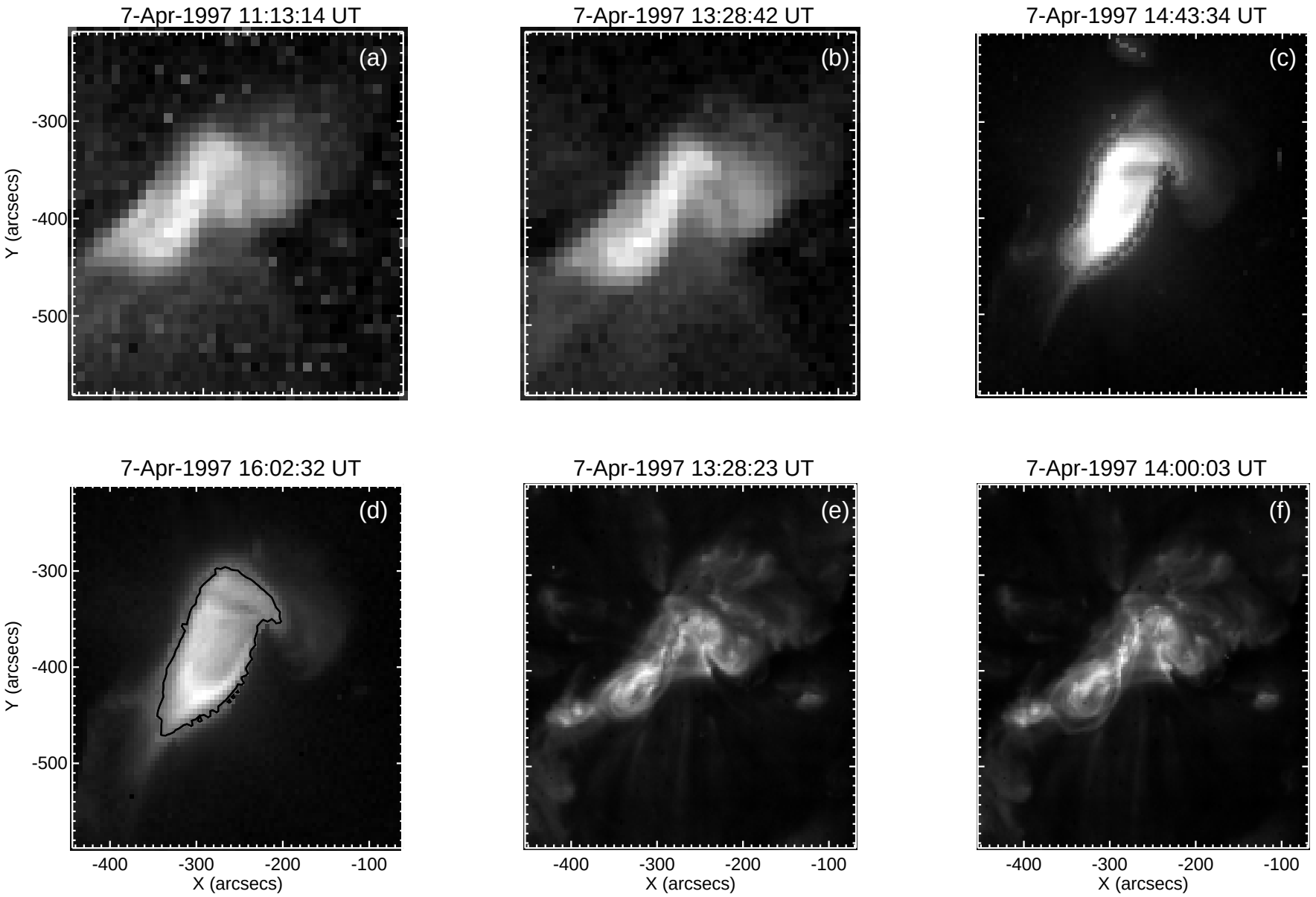

FIG. 3.—Same as Fig. 2, except for the 1997 April 7 event in SXRs for (*a*)–(*d*) and EUV in (*e*)–(*l*). The contour in (*d*) is at 5% of the maximum intensity and is used in Fig. 7.

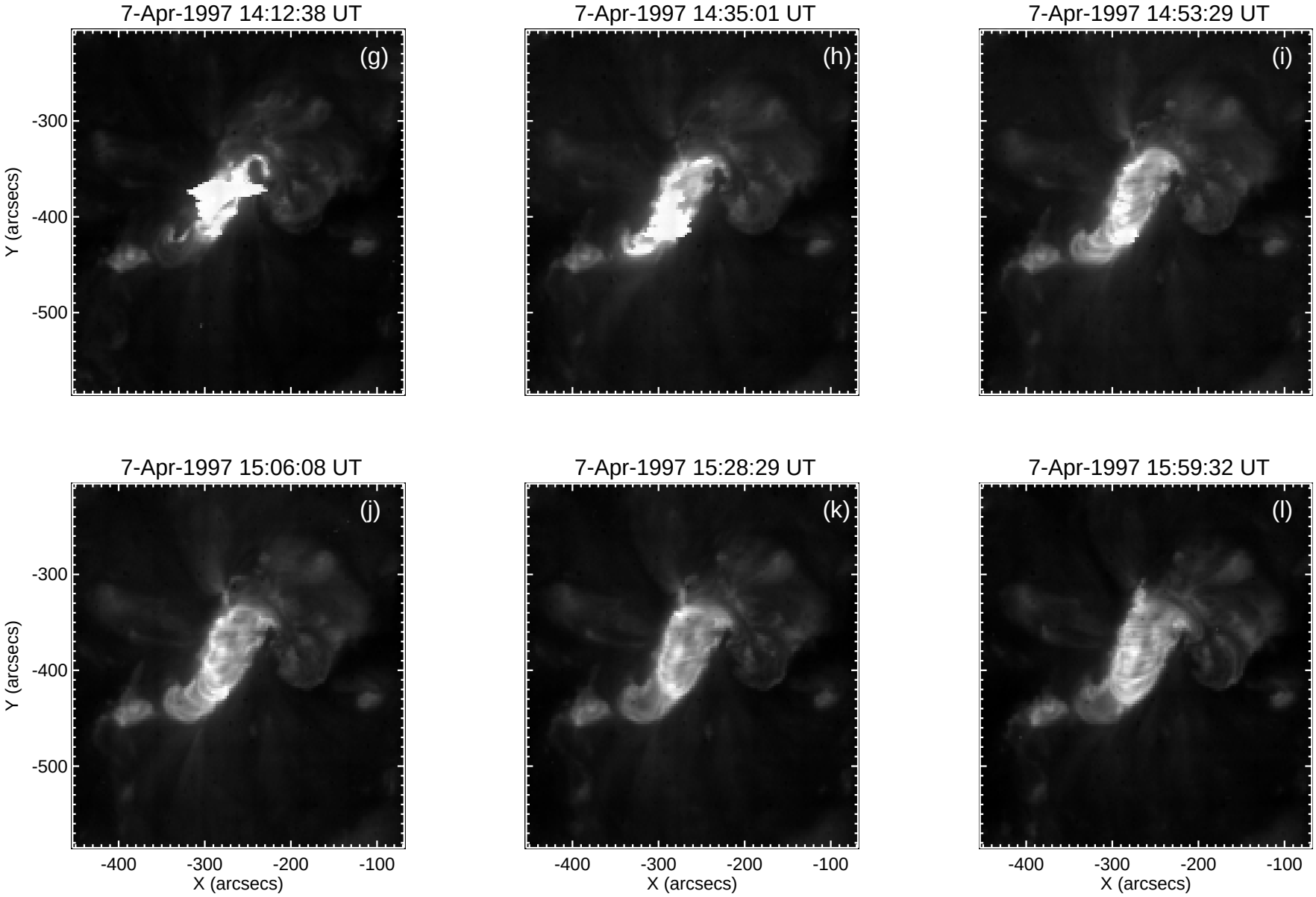

FIG. 3.—*Continued*

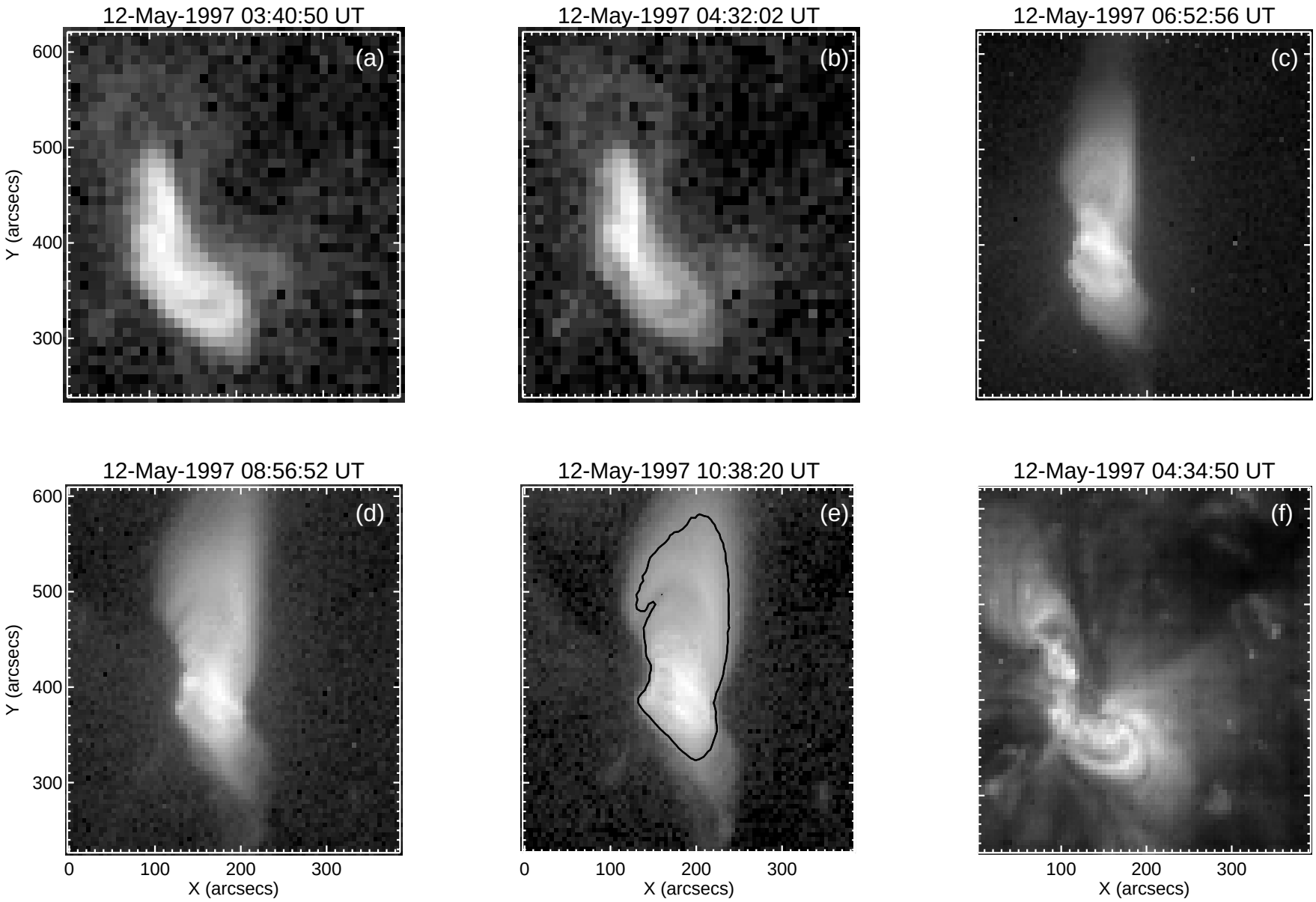

FIG. 4.—Same as Fig. 2, except for the 1997 May 12 event in SXRs for (*a*)–(*e*) and EUV in (*f*)–(*l*). The contour in (*e*) is at 5% of the maximum intensity and is used in Fig. 7.

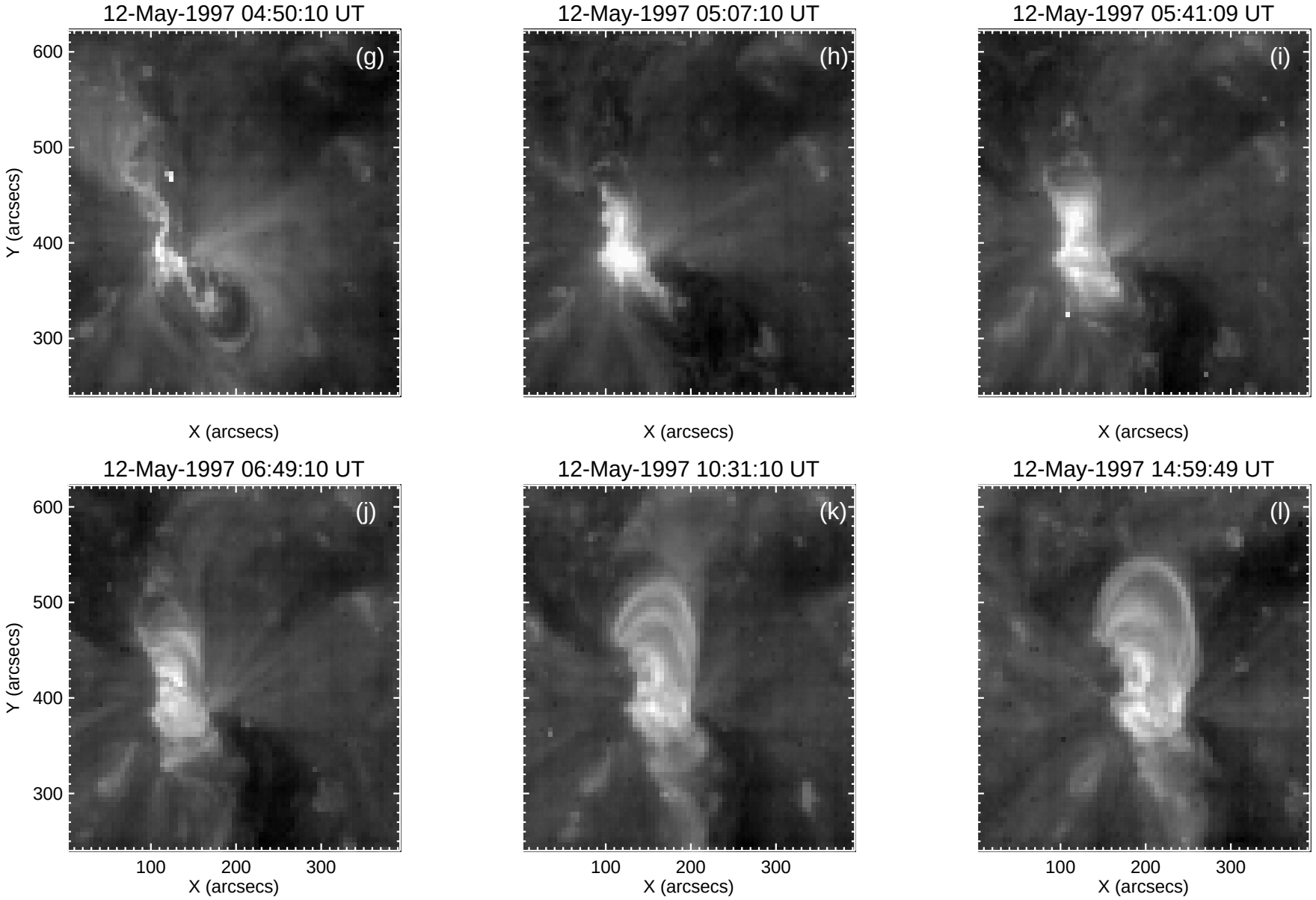

FIG. 4.—*Continued*

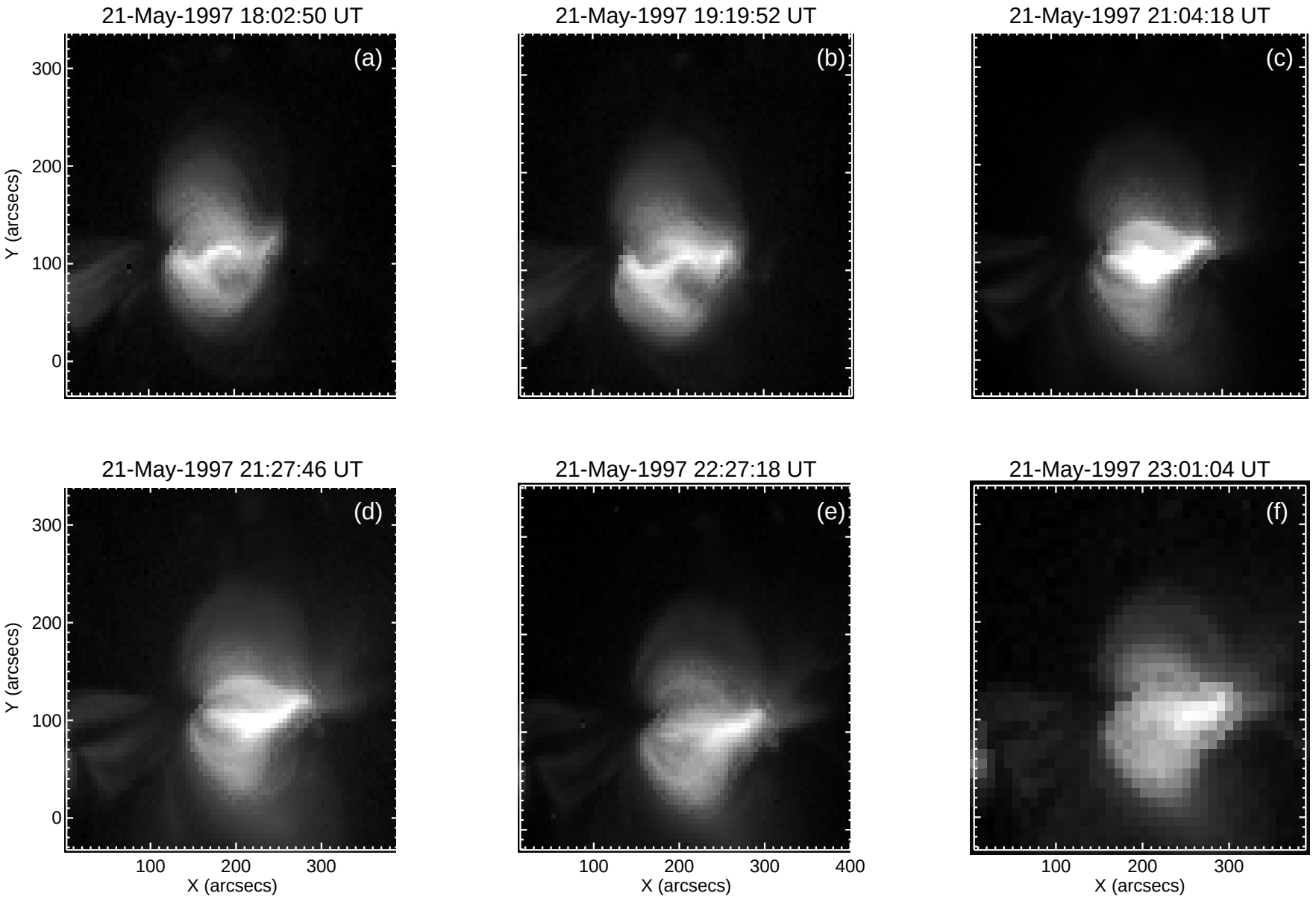

FIG. 5.—Same as Fig. 2, except for the 1997 May 21 event in SXRs for (*a*)–(*f*) and EUV in (*g*)–(*l*).

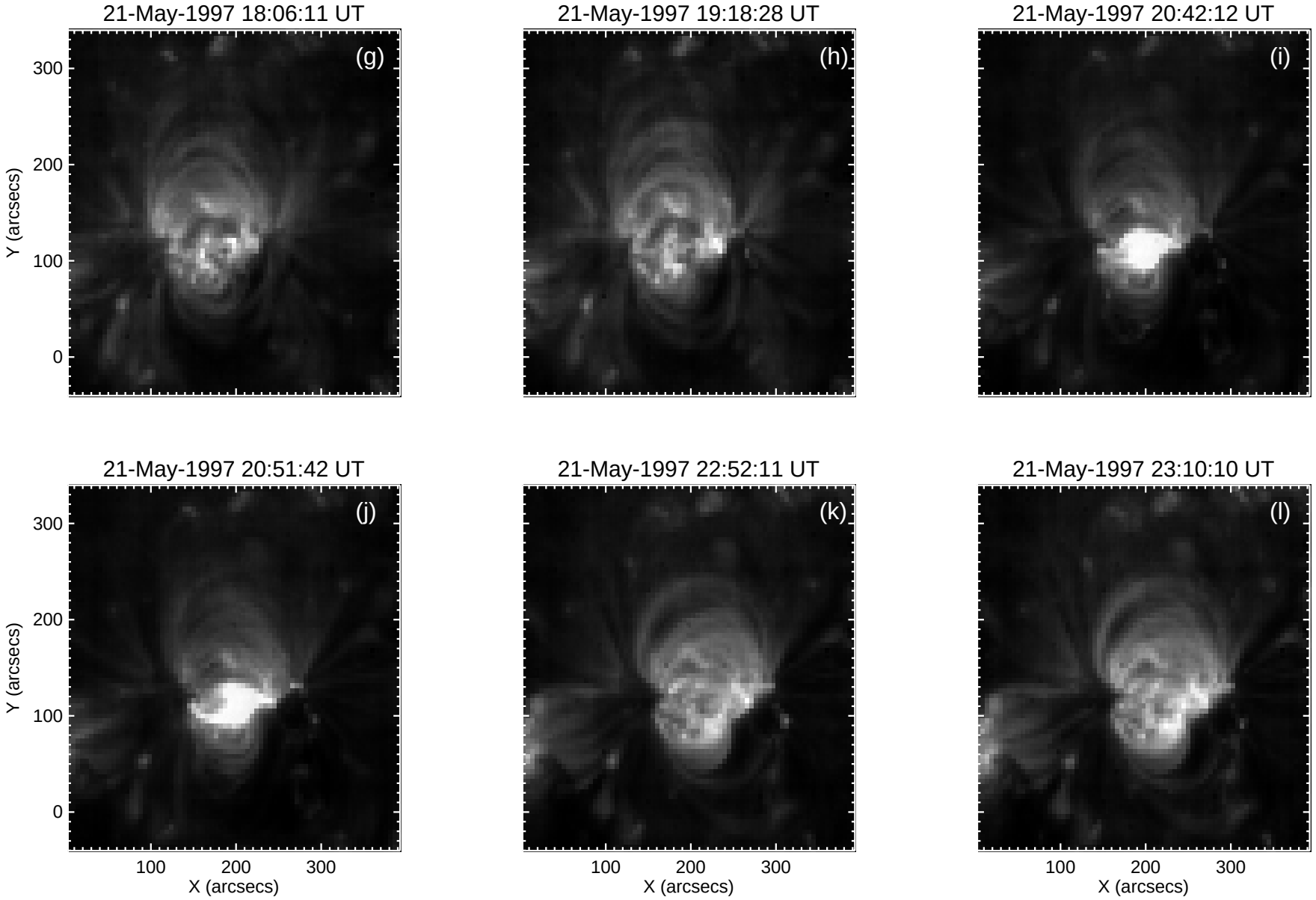

FIG. 5.—*Continued*

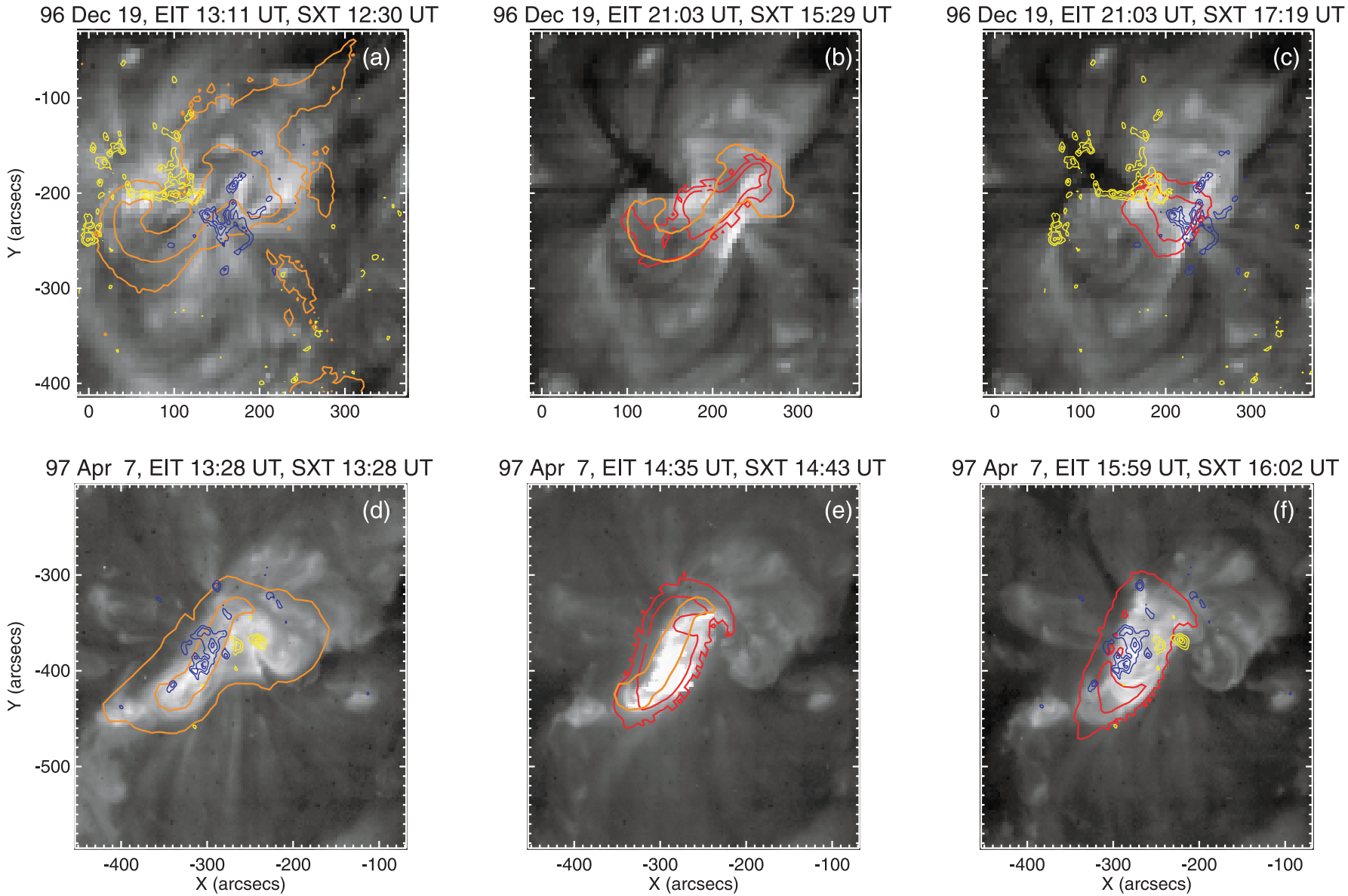

FIG. 6.—EIT images for 1996 December 19—(*a*)–(*c*); 1997 April 7—(*d*)–(*f*); 1997 May 12—(*g*)–(*i*); and 1997 May 21—(*j*)–(*l*). The leftmost column images are from preflare times, the middle images are from times during the flare (except for the December 19, which uses a postflare image for the middle image since there was no EIT image during the flare), and the rightmost column contains images from postflare times. Orange and red contours are overlays of SXT images. For the leftmost and rightmost columns, these overlays are at the SXT times listed above the panels. For the middle column, the red contours are from the SXT times listed above the image, and the orange contour is at the time of the innermost contour of the corresponding leftmost panel—i.e., the orange contour in (*b*), (*e*), (*h*), and (*k*) are identical to the innermost contours in (*a*), (*d*), (*g*), and (*j*), respectively). The contour levels are at 5%, and 25% of maximum intensity for (*a*)–(*c*), and at 5%, and 50% levels for (*d*)–(*l*). Size scales are given in arcseconds centered on solar disk center, with north at the top and east to the left, as in all the figures. Yellow and purple are opposite polarities from MDI magnetograms at contour levels of 20%, 40%, 70%, and 90% of the respective maximum values. MDI magnetograms in (*a*) and (*c*) are at 1996 December 19, 12:48 UT; in (*d*) and (*f*) at 1997 April 7, 14:27 UT; in (*g*) and(*i*) at 1997 May 12, 08:04 UT; and in (*j*) and (*l*) at 1997 May 21, 19:16 UT. Random uncertainties are dominated by a 10″ uncertainty in the pointing of EIT.

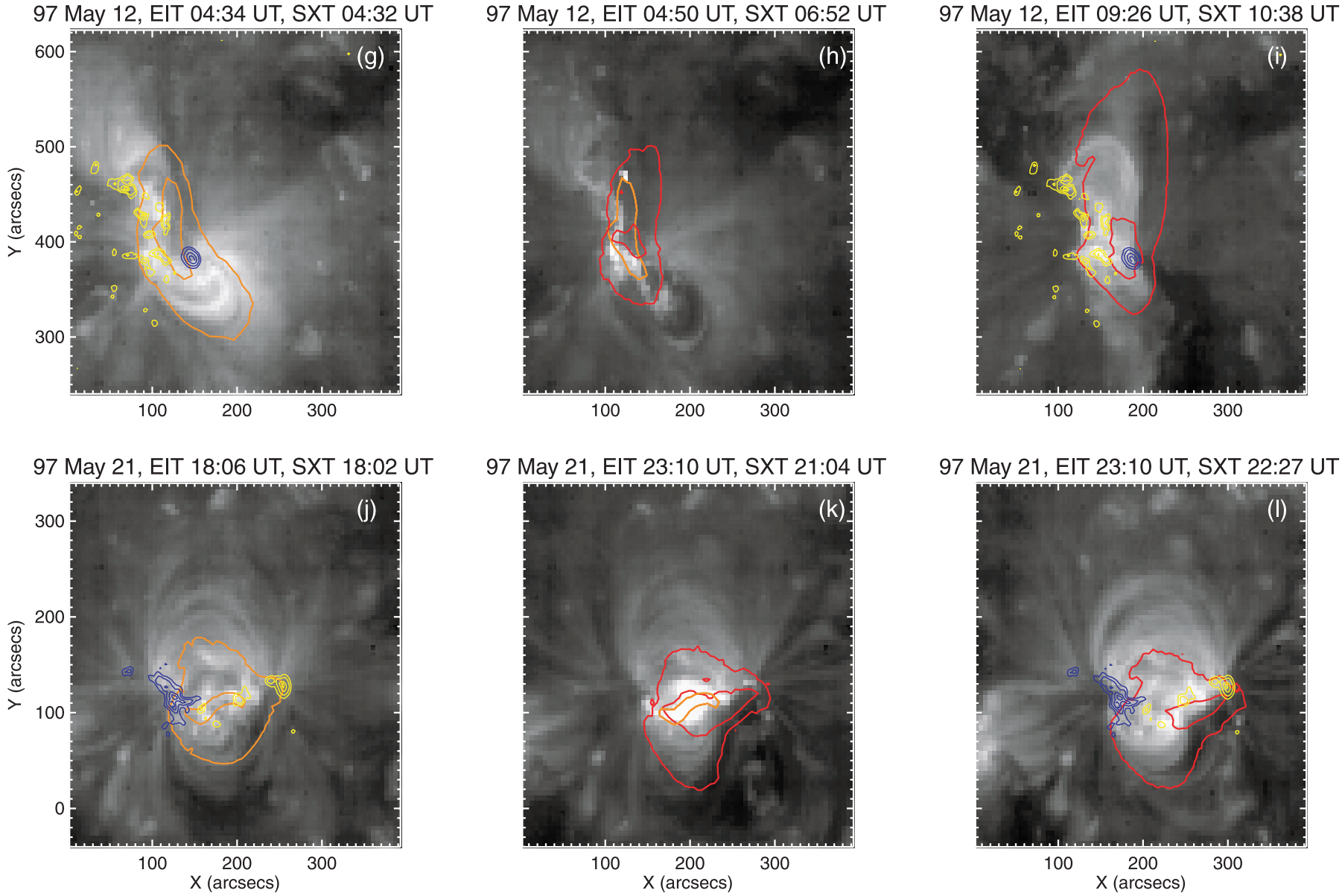

FIG. 6.—*Continued*

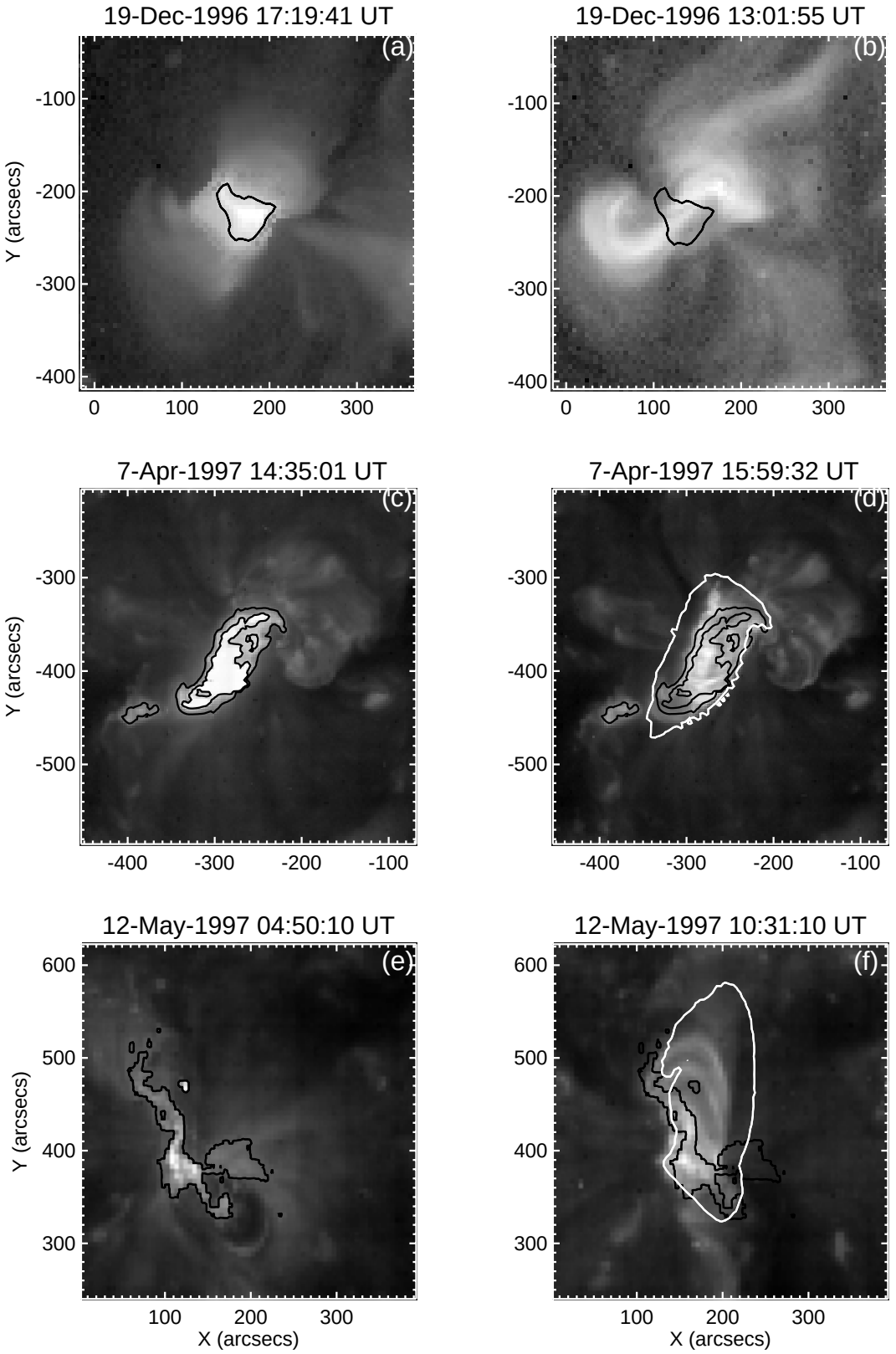

FIG. 7.—(*a*) Postflare SXT image of the 1996 December 19 event, with a contour at 25% of maximum intensity indicating the principal postflare loop structures. (*b*) Overlay of the contour (translated to compensate for solar rotation) of (*a*) onto the preflare SXT sigmoid structure. (*c*) EIT image for the 1997 April 7 event at the time of the flare overlaid with 50% and 10% intensity contours; these contours serve as proxies for the preflare SXT sigmoid structure. (*d*) The light contours are the contours of (*c*) overlaid onto a postflare EIT image. The dark contour is a 5% intensity SXT contour from the image in Fig. 3*d*. (*e*) EIT image for the 1997 May 12 event at the time of the flare overlaid with a 10% intensity contour. (*f*) The light contour is the contour of (*e*) overlaid onto a postflare EIT image. The dark contour is a 5% intensity SXT contour from the image in Fig. 4*e*.

evidence of the SXR sigmoid in Figures 5*g* and 5*h*. Brightenings with shapes similar to the SXR sigmoid occur at later times (Figs. 5*i* and 5*j*), although they do not mimic the preflare sigmoid shape exactly. We recall, however, that the EUV sigmoids in the April 7 and May 12 events were most prominent near the time of peak SXR intensity, whereas in this case our EIT images during the flare are somewhat past the time of peak intensity (cf. Fig. 1, but this statement is uncertain because of the timing problem noted at the end of § 2). Late in the flare (Figs. 5*k* and 5*l*), the region appears similar to EIT in the preflare state (Figs. 5*g* and 5*h*), although the west side of the region shows more activity than the east side, corresponding to the brighter SXR loops being on the west side of the region at these times.

We compare the images with MDI magnetograms in Figures 6*j*–6*l*. In the preflare stage (Fig. 6*j*), the SXR sigmoid does not appear to follow the neutral line, which contrasts with the three previous cases where the sigmoid followed the neutral line for a substantial part of its length. Nonetheless, there is a "kink" in the sigmoid that appears near the polarity inversion location; hence, this event may be a weaker example of a general pattern of the sigmoid following the neutral line seen in the other events. During the decay phase, the SXR structures are much less kinked, indicative of a more potential structure.

4. GEOMETRY OF PRE-EVENT AND POST-EVENT STRUCTURES

A key to understanding how the preeruption sigmoid structures evolve into the post-event structures is determining the geometric relationship between them. One of the most fundamental geometric questions is the relationship between the footpoints of these features. We address this question using the first three of our events. For the May 21 event, the changes in the preflare and postflare loop structures were not sufficiently pronounced to easily identify differences in footpoint locations.

Because of the high electrical conductivity in and above the photosphere, we expect field lines to remain tied to photospheric motions. Hence flux transfer or reconnection in the corona should correspond to changes in the links between photospheric footpoints involving different coronal structures. Therefore, determining whether preflare and postflare structures have different footpoints has implications on whether the postflare structures evolve into or reconnect to form the postflare structures or if the field lines of the structures at the two times are totally disjoint.

Figures 7*a* and 7*b*, respectively, show post-event and pre-event SXT images of the December 19 event. From the intensity contour of the post-event structures in Figure 7*a*, we identify the approximate locations where the most intense postflare loops intersect the solar surface as the northeastern tip (i.e., toward the upper left-hand corner in the image) of the contour and the broad southwestern side of the contour. Comparing with Figure 6*c* shows that these locations are rooted in regions of opposite magnetic polarity. Figure 7*b* shows the same contour (rotated to compensate for solar rotation) overlaid onto the preeruption sigmoid. To within the 10″ EIT positional uncertainties (SXT positional uncertainties are substantially smaller) of the overlay, the footpoints of the two structures are completely disjoint, thus supporting our hypothesis in § 3.1 that the postflare loops are a new structure oriented normal to the original sigmoid. They are not simply an intensification and reorganization of loops easily visible in the sigmoidal preflare images, and they do not represent reconnected field lines from the preflare sigmoid.

We compare the footpoint locations of the April 7 and May 12 events based mainly on EIT images rather than SXT images since only lower resolution SXT images (9.″8 pixel^{-1} instead of 4.″9 pixel^{-1}) from the preflare phase are available in these cases. Figure 7*c* shows an image during the main phase of the April 7 flare overlaid with 50% and 10% EUV intensity contours of the same image. We identify the EUV preflare sigmoid based on the observation (§ 3) that the brightenings in EUV during the flare are spatially correlated with the preflare SXR sigmoid (cf. Fig. 6*e*). In Figure 7*c*, we associate the preflare sigmoid with the locations of the northwestern and southeastern tips of the intensity contours. Overlying these contours onto the postflare EIT image in Figure 7*d* indicates that these footpoint locations are separate from the developing EUV arcade. In particular, the postflare arcade appears to be composed of loops overlying the preflare sigmoid and anchored in the surface on either side of the preflare sigmoid location. In Figure 7*d*, we have added a 5% contour of the SXT image in Figure 3*d* (which also shows the same contour). That added SXR contour is from approximately the same time as the EIT image in Figure 7*d* and shows that the SXR loops envelop the EUV loops (Zarro et al. 1999). Again, different magnetic field lines appear to be connected to the preflare sigmoid and the postflare arcade.

Figures 7*e* and 7*f* are analogous to Figures 7*c* and 7*d*, but for the May 12 event. In this case, it is difficult to identify the preflare sigmoid in the EUV contour. The identification of footpoints is ambiguous, and we cannot readily distinguish sigmoid and arcade field lines. General features of Figure 7*f*, however, are similar to those of Figure 7*d*, in which postflare EUV arcade loops overlie the location of the preflare sigmoid (as indicated by the EUV contour), with the arcade footpoints rooted in the surface at different locations from the preflare sigmoid. A low-lying SXR arcade and SXR cusplike structure overlie the EUV arcade.

From the inferred geometry, we estimate the average velocity of expansion of the developing postflare arcades for each of these events. For the December 19 event, we estimate the footpoint separation of the postflare loop system to be $\approx 60''$, which it developed over approximately 100 minutes between Figures 2*c* and 2*h*, implying an expansion velocity of about 7 km s^{-1}. For April 7, Figures 7*c* and 7*d* indicate that the EUV loops expanded a maximum of $\approx 60''$ in ≈ 90 minutes, giving ≈ 8 km s^{-1}, while the SXT loops expanded to $\approx 90''$ over this time, giving ≈ 12 km s^{-1}. Values for the May 12 event from Figures 7*e* and 7*f* are similar. These velocities may be overestimated since we do not know the initial extent of these loops that are not visible in the preflare stage. For both SXR and EUV arcades, we cannot differentiate between actual motions and apparent motions because of successive illumination of different field lines.

5. DISCUSSION

We have examined the morphological evolution of halo CME-associated soft–X-ray flares at SXR and EUV wavelengths, restricting our analysis to events showing a sigmoid-to-arcade pattern in SXRs. We dealt only with halo CMEs to increase the chance of observing the CME source regions near disk center. In addition, magnetograms of

these near–disk-center surface features have relatively small projection angles with respect to the Earth-Sun direction.

Sigmoid-to-arcade patterns appeared frequently enough in the study of halo CMEs by Hudson et al. (1998) to warrant specific investigation. Canfield, Hudson, & McKenzie (1999) show that active regions with sigmoidal patterns have a statistical preference to display "eruptive signatures." Our examined events appear to have similar morphological and temporal characteristics, thus indicating that we are observing fundamentally identical structures from different vantage points: looking directly down on the active regions for the December 19 and May 21 events and from two different directions for the April 7 and May 12 events.

We do not address the issue of the details of the preflare SXT sigmoid structure. Both the SXT and EIT images of the May 12 event hint that it may be more complex than a simple S-shaped structure, perhaps consisting of a bifurcated set of interleaved loops (two interlocked C's). April 7 seems very complex in EIT, and the SXT images may be smoother only because of poorer resolution. Pevtsov, Canfield, & Zirin (1996) also discuss complexities associated with the geometry and evolution of such structures. In any case, the key feature is that we are seeing details of the process described in § 1, whereby highly sheared preflare structures evolve into much more potential-like structures during and after the flare's occurrence.

Our examination of four events suggests the following evolutionary properties in SXRs. An initial sigmoid structure exists for some hours or days before the flare begins. It is aligned approximately along a neutral line. Some areas of the sigmoid are brighter than others. The SXR flare begins near one of the brighter portions of the preflare sigmoid and involves nearby magnetic structures separate from the sigmoid. These new structures evolve into low-lying loops with cusp-shaped structures above. The postflare loops have footpoints rooted in opposite polarity regions and are oriented normal to the neutral line (and therefore normal to the location of the preflare sigmoid). The arcade and cusp structure grows in time during the early decay phase of the flare. Rust & Kumar (1996) also showed an example from 1992 March 28 of the transformation of a sigmoid into an arcade in SXT, which basically exhibits a morphology consistent with what we find. Also, the "sinuous emission feature" of Sheeley et al. (1975) (cf. § 1) was similar to our sigmoids in that it was aligned along a neutral line; it also was associated with a filament aligned along the same neutral line, similar to our April 7 event.

From EIT 195 Å image observations, our study suggests the following evolution. Prior to the flare, an EUV sigmoid may not necessarily be observed. If present, the EUV sigmoid emission is weaker (relative to the active-region background) than the SXR sigmoid. As the flare begins, a thin EUV sigmoid brightens at the location of the SXR preflare sigmoid. The emission in EUV spreads along an arcade, with a looplike feature "bubbling out." The EUV postflare loops have rounded tops and are situated beneath the cusp structure seen in SXRs.

The chief difference between the SXR and EUV morphology observations is the temperature of the emitting material. For the cases in which the preflare sigmoid is visible in SXT images but not in EIT images, we expect the sigmoid material to be substantially hotter than the 1.5 MK temperatures to which the EIT 195 Å channel is most sensitive. We have computed the SXR temperature of the preflare sigmoid for the December 19 event using the standard SXT filter ratio technique (Tsuneta et al. 1991). At approximately 14:08 UT on December 19, we find a temperature of 2.4 MK for the preflare sigmoid summed over the brightest 75% of the image (the inner contour shown in Fig. 6*a*). For the April 7 event, there were no appropriate SXT full-frame images available prior to the flare. Filter ratio data were available, however, for April 6 at 15:46 UT when the sigmoid appeared similar to just prior to its eruption on April 7. Based on these data, we obtain a temperature of 1.7 MK. If the cooler temperature persisted during the time near the time of Figures 3*b* and 3*e*, then it explains why we observe EUV structures at the same location as the SXR sigmoid for this event.

We have used mainly the EIT 195 Å Fe XII images since they have the best coverage for CME-related events. There are also a few 284 Å Fe XV EIT images available. This filter detects emission from approximately 2.0 MK material and is therefore closer to SXT's peak response compared with the 195 Å filter. Figure 8 shows a 284 Å image during the preflare period for each of the events. These images have similarities to both the corresponding SXT and 195 Å images, which is consistent with the response of the 284 Å filter being between those two. Similar to the 195 Å images, none of the 284 Å images show clear evidence of sigmoids, although some brightenings of (or related to) the sigmoid structures can be identified. Thus, at least for the four events examined here, the sigmoids are SXR features with progressively weaker signatures in Fe XV and Fe XII EUV images. SXT also has a broader passband than does EIT, and this also may affect our ability to identify a sigmoid structure more easily in the SXT images than in the EIT images.

Our morphological findings can be summarized in the schematic diagram of Figure 9. In the preflare state (Fig. 9*a*), a sigmoid straddles the region between two opposite-polarity regions with the footpoints of the sigmoid rooted in these magnetic regions. In the preflare state, the sigmoid contains material hot enough to be seen in soft X-rays and often too hot to be seen in EUV. When the region flares, the EUV sigmoid, or a closely related structure, becomes visible in EUV. After the flare (Fig. 9*b*), prominent round-top loops develop in EUV (and probably in SXRs also), and cusp-shaped features in SXR form above the round-top loops.

Figures 9*a* and 9*b* indicate how difference images—where a preflare image is subtracted from a postflare image—would appear in SXT. Since the sigmoid is either absent or very weak in the postflare stage compared with the preflare stage, it will appear as a dimmed region. If observed from above, there will be an intensity-enhanced region (caused by the cusp) surrounded on two sides by dimmed regions where the outer edges of the sigmoid were rooted. This is similar to that pattern seen in difference images of the events studied by Sterling & Hudson (1997), Hudson et al. (1998), and Zarro et al. (1999). In addition to "compact" dimming regions caused by the sigmoid, Sterling & Hudson (1997) also detected a dimming region at a relatively large separation from the preflare sigmoid (Region R3 in their Fig. 2*d*), and Manoharan et al. (1996) detected dimming regions separated on an even larger scale. These larger scale dimmings are not accounted for in the Figure 9 schematic but could be caused by outer extensions ("elbows") of the preflare sigmoid or by larger scale enveloping structures,

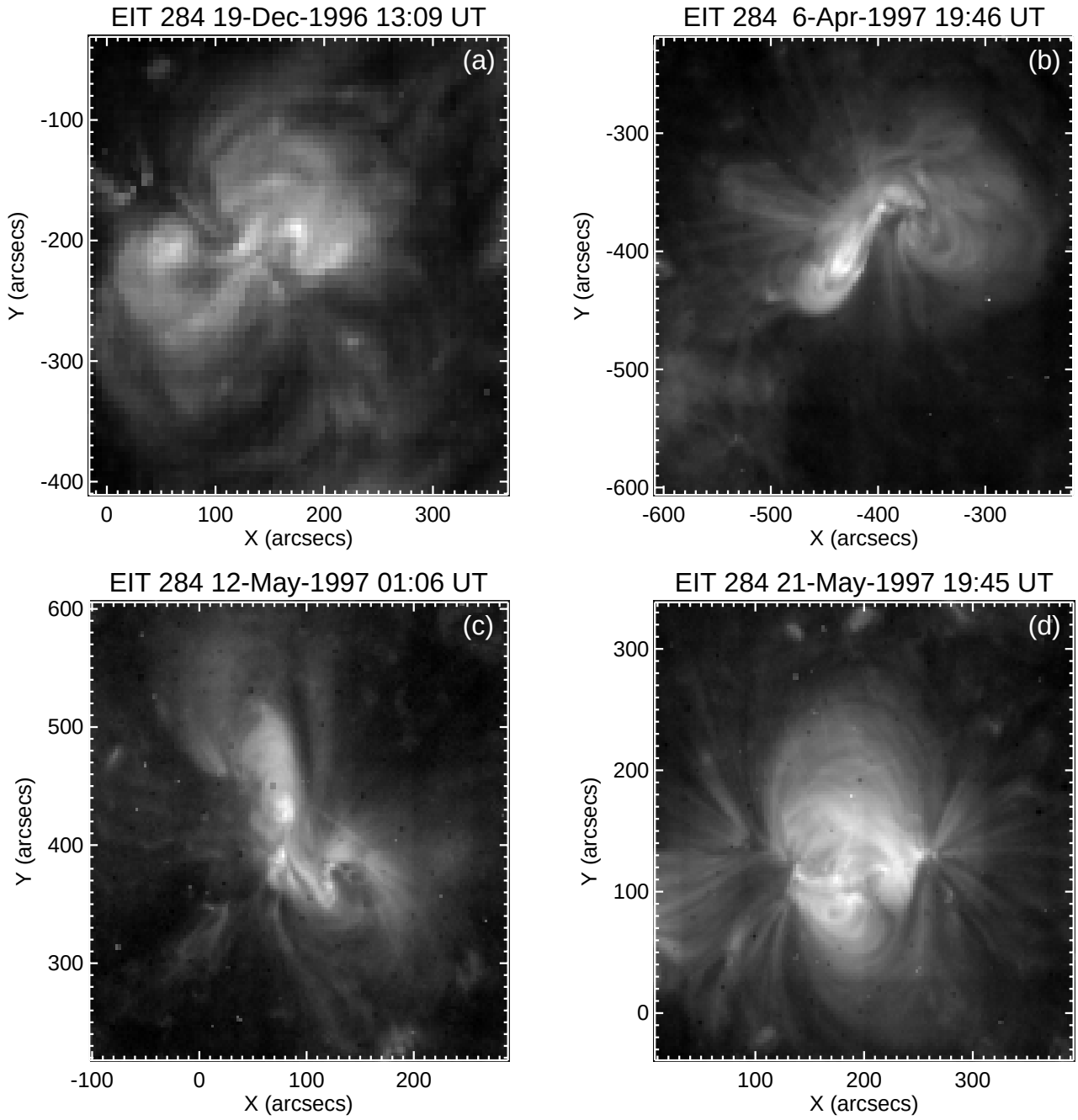

FIG. 8.—EIT 284 Å Fe XV images from preflare times of the events of (*a*) 1996 December 19, (*b*) 1997 April 7, (*c*) 1997 May 12, and (*d*) 1997 May 21. EIT images in all other figures of the paper are from the EIT 195 Å filter, which observers material at $\approx$1.5 MK. In contrast, the 284 Å filter is most sensitive to $\approx$2.0 MK material, and SXT most effectively observes material of temperatures in excess of 2–3 MK.

such as helmet streamers, that may not necessarily be related to the sigmoid.

An interpretation of these observations is that part or all of the preflare sigmoid has erupted, perhaps via a kink instability (e.g., Rust & Kumar 1996). As it leaves, it pulls field lines into the cusp-shaped loops seen in Figure 9*b*. The erupting sigmoid would leave the Sun to form part of the CME, perhaps taking the form of, or driving, a magnetic cloud (e.g., Burlaga et al. 1981; Marubashi 1986; Gosling et al. 1991; Gopalswamy et al. 1998). If only a portion of the sigmoid erupted, there would be a remnant of the original sigmoid still residing in the postflare stage. The cusp would emit in SXRs if it were heated as it was stretched upward, and perhaps reconnected, at the top of the cusp. Reconnected field lines, if shrinking slowly enough, would appear as a bright cusp in SXR or EUV emission (Forbes & Acton 1996). This interpretation is generally consistent with the standard reconnection model for flares and CMEs (e.g., Carmichael 1964; Hirayama 1974; Kopp & Pneuman 1976; Moore & Labonte 1979). In the April 7 case, we observe that the region near a preflare filament brightens, signaling the start of the eruption corresponding to the flare and CME. This observation is consistent with a flux rope being expelled from the sigmoid region and contributing to the mass of the CME (Sterling & Hudson 1997). We do not know if the eruption of the sigmoid is complete or partial, but filaments show both types of behavior (e.g., Tang 1986).

Subject to the limitations of our analysis in § 4, we find

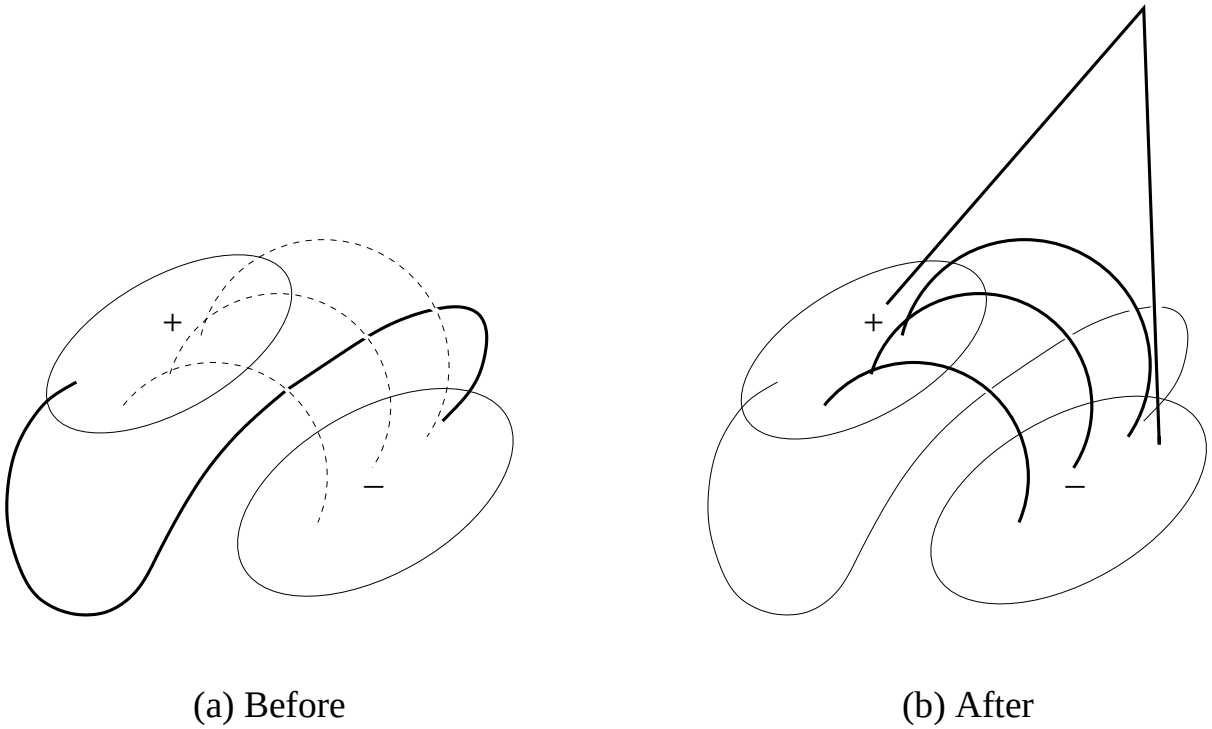

FIG. 9.—Sketch summarizing morphological properties of sigmoid-to-arcade SXT and EIT observations. (*a*) Preflare, with sigmoid structure rooted in opposite polarity regions and body following the magnetic inversion line. (*b*) Postflare, with the sigmoid structure dimmed or absent, bright rounded-top loops seen in EIT and SXT, and a bright cusp structure seen in SXT. The dashed loops in preflare sketch (*a*) are not observed, but their presence could explain the formation of the cusp and arcade if the sigmoid structure erupts.

that the footpoints of the cusp structure are distinct from those of the sigmoid. This implies that the loops that deform into the cusp are loops that were overlying (and perhaps restraining) the sigmoid in the pre-event stage. There are, however, other unresolved issues. First, why do the postflare EUV loops have rounded tops instead of cusped tops, as would be expected if they originate from the magnetic field lines originally above the preflare sigmoid? Second, why do we not observe preflare loops overlying the sigmoid prior to eruption (dashed lines in Fig. 9*a*)?

Regarding the first issue, one possibility is as suggested in standard reconnection models for flares, whereby reconnected field lines near the cusp shrink and become rounded loops. These loops would be visible initially in SXRs, and then cool to become visible in EUV (see, e.g., Svestka et al. 1987; Forbes & Acton 1996; Hori et al. 1998). This view predicts that an upward-moving reconnection point would lead to expanding loops below a growing cusp, as is observed in the events of this study.

An alternative possibility is that there is a second set of preflare loops located *below* the preflare sigmoid. Those low-lying loops would not necessarily form a cusp after the sigmoid's eruption but, via some unknown process, would be heated so that they emit in SXRs and EUV following eruption. A second alternative possibility—one that does not rely on preflare loops below the sigmoid but does assume preflare loops above the sigmoid—is that only one of the ends of the preflare sigmoid erupts, resulting in a cusp at only one end of the arcade. The remainder of the loops in the postflare arcade are predominately rounded at the tops because they are not stretched by the eruption. This scenario is suggested in an event studied by Khan et al. (1998), who found that only one end of the flare arcade formed a cusp. According to this interpretation, part of the field associated with the preflare sigmoid is restrained underneath the EUV loops after eruption but does not necessarily brighten in SXRs because some of its mass escapes along the "open" field lines of the erupting portion of the sigmoid. A third alternative possibility is that only a fraction of the sigmoid field lines erupt as in the "breakout" model (Antiochos 1998 and Antiochos, DeVore, & Klimchuk 1999), leaving behind residual lower lying loops with rounded tops.

In any of these scenarios, however, our second question remains unexplained; we do not know why there is no evidence of the putative field lines that overlie the sigmoid structure in the preflare images, i.e., the dashed lines in Figure 9*a*. They may be present but not prominent until they are ignited somehow by the erupting sigmoid.

This work is a product of a *SOHO*/*Yohkoh* Coordinated Data Analysis Workshop (CDAW) held at ISAS, in Sagamihara, Kanagawa, Japan, 1998 April 6–10. We thank B. LaBonte for useful comments on the manuscript. A. C. S. received support from the Naval Research Laboratory/Office of Naval Research basic research program. He carried out the bulk of this work while at the Institute for Space and Astronautical Science, Sagamihara, Kanagawa, Japan. A portion of this work was completed while he held a National Research Council-NASA/MSFC Research Associateship. NASA supported the work of HSH via contract NAGW-4578. D. M. Z. was supported by NAS 5-32350. *SOHO* is a project of international cooperation between ESA and NASA, and *Yohkoh* is a mission of the Institute of Space and Astronautical Sciences (Japan), with participation from the United States and the United Kingdom.

REFERENCES

Antiochos, S. K. 1998, ApJ, 502, L181
Antiochos, S. K., DeVore, C. R., & Klimchuk, J. A. 1999, ApJ, 510, 485
Berdichevsky, D., et al. 1998, Geophys. Res. Lett., 25, 2473
Brueckner, G. E., et al. 1995, Sol. Phys., 162, 357
Burlaga, L. F., et al. 1981, J. Geophys. Res., 86, 6673
———. 1998, J. Geophys. Res., 103, 277
Canfield, R. C., Hudson, H. S., & McKenzie, D. E. 1999, Geophys. Res. Lett., 26, 627
Carmichael, H. 1964, in AAS-NASA Symp. on the Physics of Solar Flares, ed. W. N. Hess (NASA-SP 50), 451
Chen, J. 1997, Coronal Mass Ejections, ed. N. Crooker, J. Joselyn, & J. Feynman (Washington: AGU), 65
Delaboudiniere, J.-P., et al. 1995, Sol. Phys., 162, 291
Dere, K. P., et al. 1997, Sol. Phys., 175, 601
Forbes, T. G., & Acton, L. W. 1996, ApJ, 459, 330
Fox, N. J., Peredo, M., & Thompson, B. J. 1998, Geophys. Res. Lett., 25, 2461
Gopalswamy, N., et al. 1998, Geophys. Res. Lett., 25, 2485
Gosling, J. T. 1996, ARA&A, 34, 35
Gosling, J. T., McComas, D. J., Phillips, J. L., & Bame, S. J. 1991, J. Geophys. Res., 96, 7831
Hirayama, T. 1974, Sol. Phys., 34, 323
Hori, K., Yokoyama, T., Kosugi, T., & Shibata, K. 1998, ApJ, 500, 492
Howard, R. A., et al. 1997, in Coronal Mass Ejections, ed. N. Crooker, J. Joselyn, & J. Feynman (Washington: AGU), 17
Howard, R. A., Michels, D. J., Sheeley, N. R., & Koomen, M. J. 1982, ApJ, 263, L101
Hudson, H. S., Lemen, J. R., St. Cyr, O. C., Sterling, A. C., & Webb, D. F. 1998, Geophys. Res. Lett., 25, 2481
Hudson, H. S., & Webb, D. F. 1997, in Coronal Mass Ejections, ed. N. Crooker, J. Joselyn, & J. Feynman (Washington: AGU), 27
Hundhausen, A. J. 1993, J. Geophys. Res., 98, 13177
Kahler, S. 1977, ApJ, 214, 891
———. 1992, ARA&A., 30, 113
Kaiser, M. L., Reiner, M. J., Gopalswamy, N., Howard, R. A., St. Cyr, O. C., Thompson, B. J., & Bougeret, J.-L. 1998, Geophys. Res. Lett., 25, 2501
Khan, J. I., Uchida, Y., McAllister, A. H., Mouradian, Z., Soru-Escaut, I., & Hiei, E. 1998, A&A., 336, 753
Kopp, R. A., & Pneuman, G. W. 1976, Sol. Phys., 50, 85
Low, B. C. 1997, Sol. Phys., 167, 217
Manoharan, P. K., van Driel-Gesztelyi, L., Pick, M., & Demoulin, P. 1996, ApJ, 468, L73
Marubashi, K. 1986, Adv. Space Res., 6(6), 335
McAllister, A. H., Dryer, M., McIntosh, P., Singer, H., & Weiss, L. 1996, J. Geophys. Res., 101, 13497
Moore, R. L., & LaBonte, B. 1979, in Solar and Interplanetary Dynamics (Dordrecht: Reidel), 207
Pevtsov, A. A., Canfield, R. C., & Zirin, H. 1996, ApJ, 473, 533
Plunkett, S. P., et al. 1998, Geophys. Res. Lett., 25, 2477
Reiner, M. J., Kaiser, M. L., Fainberg, J., Bougeret, J.-L., & Stone, R. G. 1998, Geophys. Res. Lett., 25, 2493
Rust, D. M. 1996, in ASP Conf. Proc. 111, Magnetic Reconnection in the Solar Atmosphere, ed. R. D. Bentley, & J. T. Mariska (San Francisco: ASP), 353
———. 1997, in Coronal Mass Ejections, ed. N. Crooker, J. Joselyn, & J. Feynman (Washington: AGU), 119
Rust, D. M., & Hildner, E. 1976, Sol. Phys., 48, 381
Rust, D. M., & Kumar, A. 1996, ApJ, 464, L199
Sakurai, T., Shibata, K., Ichimoto, K., Tsuneta, S., & Acton, L. 1992, PASJ, 44, L123
Scherrer, P. H., et al. 1995, Sol. Phys., 162, 129
Sheeley, N. R., Jr., et al. 1975, Sol. Phys., 45, 377
Sterling, A. C., & Hudson, H. S. 1997, ApJ, 491, L55
Svestka, Z. F., Fontenla, J. M., Mackado, M. E., Martin, S. F., & Neidig, D. F. 1987, Sol. Phys., 108, 237
Tang, F. 1986, Sol. Phys., 105, 399
Thompson, B. J., et al. 1999, ApJ, 517, L151
Thompson, B. J., Plunkett, S. P., Gurman, J. B., Newmark, J. S., St. Cyr, O. C., & Michels, D. J. 1998, Geophys. Res. Lett., 25, 2465
Tsuneta, S., et al. 1991, Sol. Phys., 136, 37
Tsuneta, S., Hara, H., Shimizu, T., Acton, L. W., Strong, K. T., Hudson, H. S., & Ogawara, Y. 1992, PASJ, 136, 37
Watari, S., & Watanabe, T. 1998, Geophys. Res. Lett., 25, 2489
Webb, D. F., Cliver, E. W., Gopalswamy, N., Hudson, H. S., & St. Cyr, O. C. 1998, Geophys. Res. Lett., 25, 2469
Zarro, D. M., Sterling, A. C., Thompson, B. J., Hudson, H. S., & Nitta, N. 1999, ApJ, 520, 139